Controls on the isotopic composition of microbial methane

Jonathan Gropp,[1*] Qusheng Jin,[2] Itay Halevy[1]

[1]Department of Earth and Planetary Sciences, Weizmann Institute of Science, Rehovot, Israel

[2]Department of Earth Sciences, University of Oregon, Eugene, Oregon, USA

[*]To whom correspondence should be addressed; E-mail: jonathan.gropp@weizmann.ac.il.

Abstract

Microbial methane production (methanogenesis) is responsible for more than half of the annual emission of this major greenhouse gas to the atmosphere. Though the stable isotopic composition of methane is often used to characterize its sources and sinks, empirical descriptions of the isotopic signature of methanogenesis currently limit such attempts. We developed a biochemical-isotopic model of methanogenesis by CO_2 reduction, which predicts carbon and hydrogen isotopic fractionations, and clumped isotopologue distributions, as functions of the cell's environment. We mechanistically explain multiple-isotopic patterns in laboratory and natural settings and show that such patterns constrain the in-situ energetics of methanogenesis. Combining our model with environmental data, we infer that in almost all marine environments and gas deposits, energy-limited methanogenesis operates close to chemical and isotopic equilibrium.

Methane (CH_4) is a major greenhouse gas, with both natural and anthropogenic sources (*1*). The primary natural source of biogenic methane emissions is archaeal methanogenesis in anoxic environments (*2*), about a third of which is hydrogenotrophic (reduction of CO_2 with dihydrogen, H_2; Ref. *3*). Strong isotopic discrimination during biological and abiotic methane formation has motivated the use of methane hydrogen and carbon isotopes to trace its production and consumption processes, construct global methane budgets and evaluate its climatic impacts (*1*, *4*, *5*). Current organism-level models that rely on isotopic mass balance can explain part of the observed range of microbial isotopic discrimination (*6–9*), but to date, such models have prescribed rather than resolved the microbial biochemistry. It has been difficult, therefore, to distinguish between different methane sources, different modes and extents of environmental methane cycling, and different environmental controls on the microbial isotope discrimination as drivers of observed variations in the isotopic composition of methane. To constrain the microbial component of such variations, we developed and analyzed a full metabolic-isotopic model of hydrogenotrophic methanogenesis, which predicts the isotopic discrimination and its relation to the thermodynamic drive of this pathway (the Gibbs free energy of the net reaction $4H_2 + CO_2 \rightleftharpoons CH_4 + 2H_2O$, ΔG_{net}) and to cell-specific methanogenesis rates in laboratory cultures. Extending our analysis to energy-limited conditions, which are prevalent in natural environments, our model reveals the environmental and metabolic controls on the isotopic composition of methane.

Accounting for the kinetics and thermodynamics of enzymatically-catalyzed reactions in hydrogenotrophic methanogenesis (details in the Supplementary Materials, SM), we constructed mass balance equations for the intracellular metabolites in the pathway (Fig. 1A). Given extracellular concentrations of CO_2, H_2 and CH_4, and pH, which define ΔG_{net}, these equations are solved for the steady-state concentrations of the intracellular metabolites (fig. S1). At this steady state, the model links metabolite concentrations to the net rate of methanogenesis, and to the gross forward and reverse rates of the individual reactions. We calibrated our metabolic model to available measurements of specific methanogenesis rates and their relation to H_2 concentrations in the μM to mM range (fig. S2; SM). The metabolic model accounts for electron transfer from H_2 to the in-

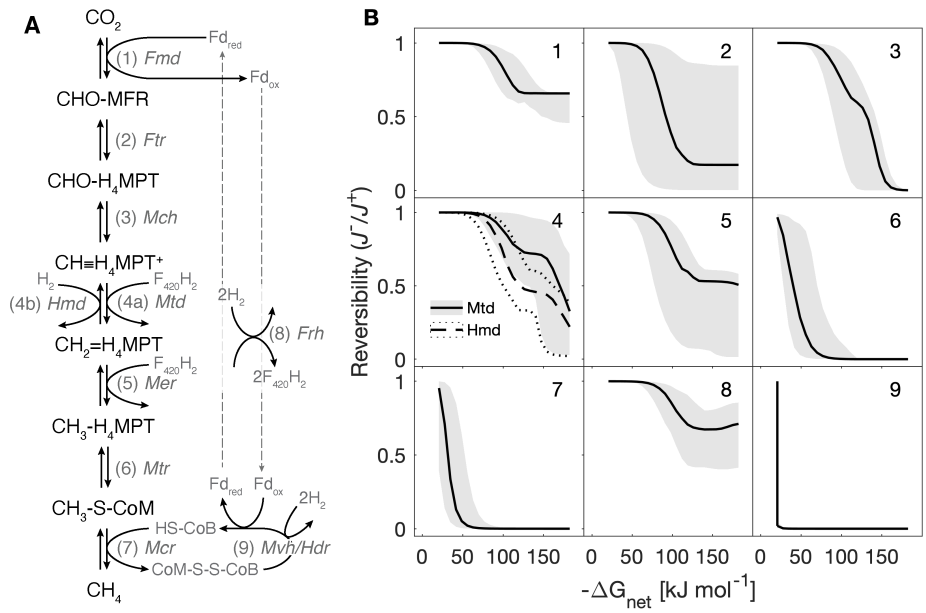

Figure 1: A metabolic model of hydrogenotrophic methanogenesis. (**A**) Schematic pathway. Abbreviated enzyme names are in italics (table S1). (**B**) Individual reaction reversibility (J_i^-/J_i^+) against ΔG_{net}. The subplots in panel B are numbered in accordance with panel A and table S1. The black lines are the median of 10^3 model simulations, and envelopes represent 95% of model results. The uncertainty originates from the enzyme kinetic parameters. Simulations were carried out at [H_2] of 1 nM to 10 mM, and typical experimental [CO_2] and [CH_4] of 10 mM and 10 μM, respectively.

termediate metabolites through three electron carriers, cofactor F_{420}, coenzyme B (HS-CoB), and ferredoxin (Fd), and we validated the calibrated model predictions of the oxidation state of these electron carriers against available experimental and theoretical estimates (SM).

The calibrated and validated biochemical model forms the basis for the metabolic-isotopic coupling. With increasing H_2 concentrations, ΔG_{net} becomes increasingly negative, and the individual reactions in the pathway depart from equilibrium to various extents (Fig. 1B). We quantify the departure from equilibrium by the individual reaction reversibility, defined as the ratio of the reverse to forward gross rates of that reaction and related to its actual transformed Gibbs free energy, $J_i^-/J_i^+ = \exp(\Delta G_i'/RT)$ (*10–12*). For net forward methanogenesis rates, the reversibility of individual reactions varies between zero (a near-unidirectional, kinetically controlled reaction) and unity (a near-equilibrium reaction). Some reactions do not fully depart from reversibility in the explored ΔG_{net} space (e.g., the Frh-catalyzed reduction of F_{420}), whereas others depart from reversibility at

ΔG_{net} as modestly negative as –15 kJ mol^{-1} (e.g., the Mvh/Hdr, Mcr and Mtr-catalyzed reactions). This differential response is a combined function of the reaction thermodynamics, expressed as the standard-state transformed Gibbs free energy ($\Delta G_i'^0$), and the enzyme kinetics, specifically the metabolic rate capacity (V^+) and Michaelis constants (K_M). Neither $\Delta G_i'^0$ nor V^+ and K_M in isolation predict the pattern of differential departure from equilibrium—coupled thermodynamics and kinetics must be considered.

The net isotopic fractionation (α, SM) expressed in an individual (bio)chemical reaction may vary between thermodynamic equilibrium and kinetic end-members, associated respectively with a reversible reaction and unidirectional forward reaction to form the reaction product. With the reversibilities calculated in the metabolic model and with values assigned to the equilibrium and kinetic isotopic fractionation factors (EFFs and KFFs, respectively) of the individual reactions, the net isotopic fractionation between the pathway substrates and products may be calculated (*13*, *14*). We calibrated the relations between ΔG_{net} and the resulting net carbon and hydrogen isotopic fractionations against experimental data, then used the calibrated model to determine the relation between ΔG_{net} and the abundance of doubly substituted ("clumped") methane isotopologues, which has yet to be systematically explored in experiments.

In laboratory cultures, the CO_2–CH_4 carbon isotope fractionation ($^{13}\varepsilon_{CO_2\text{-}CH_4}$, where $\varepsilon = 1 - \alpha$ [‰]) is inversely related to ΔG_{net} (*8*, *15–19*, fig. S3A). At near-zero ΔG_{net}, the individual reactions in the pathway operate close to equilibrium ($J_i^- / J_i^+ \to 1$), and our model predicts $^{13}\varepsilon_{CO_2\text{-}CH_4}$ close to the temperature-dependent isotopic equilibrium fractionation ($^{13}\varepsilon^{eq}_{CO_2\text{-}CH_4}$). When ΔG_{net} becomes slightly negative, $^{13}\varepsilon_{CO_2\text{-}CH_4}$ peaks to larger-than-equilibrium values of 80-100‰ at ≈–45 kJ mol^{-1}, followed by a gradual decline to ≈30‰ reached at ΔG_{net} of ≈–120 kJ mol^{-1} (Fig. 2A). Such larger-than-equilibrium $^{13}\varepsilon_{CO_2\text{-}CH_4}$ values have been observed in several experimental and environmental datasets and have yet to be explained mechanistically. Our model reveals that this ΔG_{net}–$^{13}\varepsilon_{CO_2\text{-}CH_4}$ relation is controlled by the landscape of departure from equilibrium of the individual reactions in the pathway. The carbon reaction network in methanogenesis is linear. In such networks, near-unidirectionality of an individual reaction ($J_i^- / J_i^+ \to 0$) leads to expression

of that reaction's KFF and suppresses isotopic fractionation associated with downstream reactions (*14*). The Mcr-catalyzed reaction's KFF (≈40‰, Ref. *20*) is larger than its EFF (≈1‰, Ref. *21*). As this reaction departs from equilibrium, the peak in ${}^{13}\varepsilon_{CO_2\text{-}CH_4}$ reflects a sum of its KFF and the EFFs of upstream reactions, with the exception of the Mtr-catalyzed reaction, which also partially departs from equilibrium (Fig. 1B). The ${}^{13}\varepsilon_{CO_2\text{-}CH_4}$ floor at ΔG_{net} more negative than ≈–120 kJ mol^{-1} (Fig. 2A) is defined by partial expression of the KFFs of Ftr and Fmd, and suppression of the isotopic fractionations associated with downstream reactions.

At large-negative ΔG_{net} values ${}^{13}\varepsilon_{CO_2\text{-}CH_4}$ is sensitive also to the extracellular partial pressure of CO_2 (pCO_2). At a steady state, intracellular CO_2 utilization is exactly matched by net CO_2 diffusion across the membrane. This net diffusive flux is the difference between large gross fluxes (into and out of the cell) when pCO_2 is high, and smaller gross fluxes at lower pCO_2. Thus, the reversibility of net diffusion is low at low pCO_2, and suppression of downstream net carbon isotopic fractionation results in small ${}^{13}\varepsilon_{CO_2\text{-}CH_4}$. The dependence of ${}^{13}\varepsilon_{CO_2\text{-}CH_4}$ on pCO_2 explains the smallest net fractionations observed in laboratory cultures (lower bound of red envelope in Fig. 2B, Ref. *17*), as well as the dependence of ${}^{13}\varepsilon_{CO_2\text{-}CH_4}$ on pH in hyperalkaline settings (*22*, *23*).

The CH_4–H_2O hydrogen isotopic fractionation (${}^{2}\varepsilon_{CH_4\text{-}H_2O}$) in laboratory cultures is ≈200‰ more negative than the temperature-dependent isotopic equilibrium fractionation (${}^{2}\varepsilon^{eq}_{CH_4\text{-}H_2O}$), and existing observations suggest that it does not display a clear dependence on ΔG_{net} (*8*, *15*, *18*, *24*, *25*, fig. S3B). Unlike the linear carbon reaction network, the hydrogen reaction network has four branches, each of which has the potential for hydrogen atom exchange between pathway intermediates and H_2O. Therefore, departure from equilibrium of one of the hydrogen atom exchange reactions does not preclude CH_4-H_2O hydrogen isotopic equilibrium. Specifically, the Mvh/Hdr-catalyzed reaction is near-irreversible at ΔG_{net} values as high as –25 kJ mol^{-1} (Fig. 1B), yet at this ΔG_{net} value ${}^{2}\varepsilon_{CH_4\text{-}H_2O} \simeq {}^{2}\varepsilon^{eq}_{CH_4\text{-}H_2O}$ (Fig. 2C), and this arises from the high reversibility of the other hydrogen atom exchange reactions in the pathway. Only when the Mcr- and Mtr-catalyzed reactions sufficiently depart from reversibility ($\Delta G_{net} \leq$ –30 kJ mol^{-1}), cutting off CH_4 and HS-CoB from exchange with upstream intermediates that are close to hydrogen isotope equilibrium with

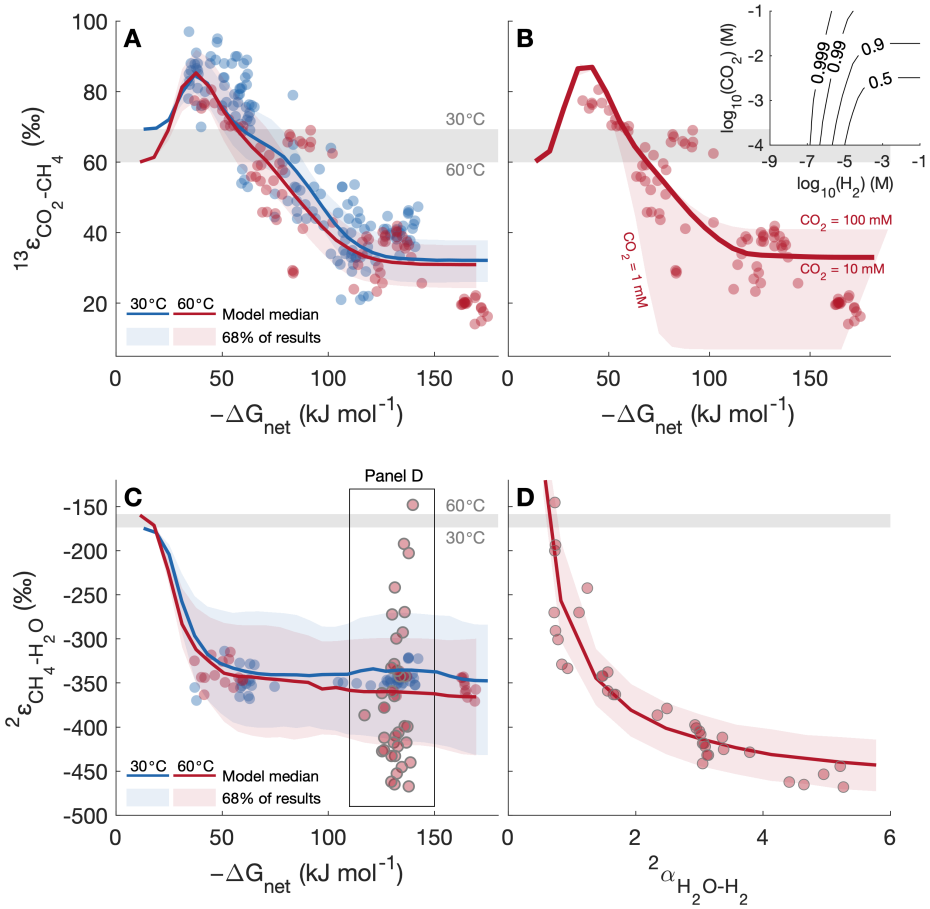

Figure 2: Model-laboratory culture comparison of bulk carbon and hydrogen isotopic fractionation. Mesophilic (30–40°C, blue circles) and thermophilic (≥55°C, red circles) experimental data and model results (lines and envelopes) at 30°C (blue) and 60°C (red), and the equilibrium isotopic fractionation (gray envelopes). (**A, C**) ${}^{13}\varepsilon_{CO_2\text{-}CH_4}$ and ${}^{2}\varepsilon_{CH_4\text{-}H_2O}$ against ΔG_{net}. (**B**) ${}^{13}\varepsilon_{CO_2\text{-}CH_4}$ against extracellular CO_2 concentrations ($[CO_{2(out)}]$). Contours in the inset show the reversibility of cross-membrane CO_2 diffusion. (**D**) Mixing effects on ${}^{2}\varepsilon_{CH_4\text{-}H_2O}$ as a function of the H_2O–H_2 isotopic fractionation (${}^{2}\alpha_{H_2O\text{-}H_2}$), compared to laboratory culture data (*8*).

H_2O, does ${}^{2}\varepsilon_{CH_4\text{-}H_2O}$ depart from ${}^{2}\varepsilon^{eq}_{CH_4\text{-}H_2O}$ (Fig. 2C). At ΔG_{net} more negative than -40 kJ mol^{-1} the KFFs of Mcr, Mtr and Mvh/Hdr control ${}^{2}\varepsilon_{CH_4\text{-}H_2O}$ (fig. S4). Overall, our model reveals a clear ${}^{2}\varepsilon_{CH_4\text{-}H_2O}$–$\Delta G_{net}$ relation, which has not been accessed by the range of ΔG_{net} explored in laboratory cultures to date. The apparent invariance of ${}^{2}\varepsilon_{CH_4\text{-}H_2O}$ at ΔG_{net} more negative than –40 kJ mol^{-1} represents a complex, ΔG_{net}-dependent combination of isotope effects associated with the enzymes in the pathway.

The hydrogen atom added to CH-H_4MPT may come from H_2O in the Mtd-catalyzed reaction, or from H_2 in the Hmd-catalyzed reaction (Fig. 1A; *26*). Thus, up to one quarter of the hydrogen atoms in methane may come from H_2, depending on the relative activity of Mtd and Hmd. High H_2 concentrations favor high methanogenesis rates and Hmd activity. Under these conditions, and especially in the case of H_2-H_2O isotopic disequilibrium, ${}^{2}\varepsilon_{CH_4\text{-}H_2O}$ may vary in response to variations in the hydrogen isotopic composition of H_2. Our model captures this behavior, as observed in culture experiments with 1 mM [H_2] and at 60°C (*8*, *25*), displaying ${}^{2}\varepsilon_{CH_4\text{-}H_2O}$ values between –145‰ and –480‰, which inversely covary with the H_2O-H_2 isotopic fractionation (Fig. 2D).

Our predicted trajectories for departure from equilibrium ${}^{13}\varepsilon_{CO_2\text{-}CH_4}$ and ${}^{2}\varepsilon_{CH_4\text{-}H_2O}$ values may explain observations of near-equilibrium ${}^{13}\varepsilon_{CO_2\text{-}CH_4}$ values concurrent with clearly disequilibrium ${}^{2}\varepsilon_{CH_4\text{-}H_2O}$ values, which have been previously explained by a decoupling of the carbon and hydrogen isotopic systems in methanogenesis (*8*, *27*). We suggest instead, that the measured ${}^{13}\varepsilon_{CO_2\text{-}CH_4}$ values did not reflect isotopic equilibrium, but the descending branch from the ${}^{13}\varepsilon_{CO_2\text{-}CH_4}$ maximum (at $\Delta G_{net} \approx$–40 kJ mol^{-1}) with increasingly negative ΔG_{net}.

The distributions of the clumped isotopologues of CH_4 ($\Delta^{13}CH_3D$ and $\Delta^{12}CH_2D_2$) depend on the methane formation temperature (*6*). However, applications of methane clumped isotopes to constrain its formation are complicated by source mixing and disequilibrium effects (*7*, *28*). The dependence of $\Delta^{13}CH_3D$ and $\Delta^{12}CH_2D_2$ on ΔG_{net} has not been determined experimentally, and similar to bulk carbon isotopes, our model predicts non-monotonic departure from clumped isotopic equilibrium (fig. S5), unlike previous estimates of these relations (*7*, *29*). As ΔG_{net} becomes negative, both $\Delta^{13}CH_3D$ and $\Delta^{12}CH_2D_2$ values decrease from the expected equilibrium compositions, and $\Delta^{12}CH_2D_2$ becomes anti-clumped (i.e., < 0‰) due to expression of the KFFs of the Mcr- and Mtr-catalyzed reactions. After the initial decrease in $\Delta^{13}CH_3D$ and $\Delta^{12}CH_2D_2$, both increase with increasingly negative ΔG_{net} to values almost as high as the equilibrium values. This behavior has two implications. First, there is a range of ΔG_{net} ($\approx$–75 to –55 kJ mol^{-1}) over which $\Delta^{13}CH_3D$ values may give the false appearance of proximity to isotopic equilibrium. Second, there is a range of ΔG_{net} ($\approx$–100 to –20 kJ mol^{-1}) over which $\Delta^{13}CH_3D$ and $\Delta^{12}CH_2D_2$ cannot uniquely

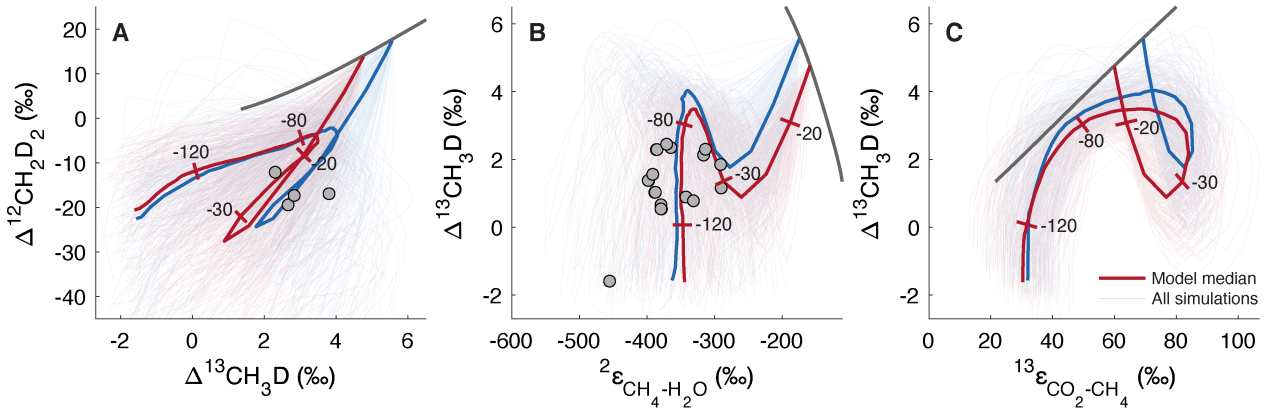

Figure 3: Model-laboratory culture comparison of clumped isotopologue abundances. Experimental data (gray circles) and model results (thin lines) of 200 simulations at 30°C (blue) and 60°C (red). The dark gray lines represent temperature-dependent isotopic equilibrium at 0-350°C, and the thick red and blue lines show the median of the individual simulations, with tickmarks at ΔG_{net} values of –20, –30, –80, and –120 kJ mol^{-1}. (**A**) $\Delta^{13}CH_3D$ against $\Delta^{12}CH_2D_2$. (**B**) $\Delta^{13}CH_3D$ against ${}^{2}\varepsilon_{CH_4\text{-}H_2O}$. (**C**) $\Delta^{13}CH_3D$ against ${}^{13}\varepsilon_{CO_2\text{-}CH_4}$. Laboratory culture samples are from hydrogenotrophic methanogens that do not have membrane-associated methanophenazines.

constrain the energetic state of the cell (e.g., $\Delta^{13}CH_3D$ is ≈4 ‰ at both ΔG_{net} of ≈–20 and ≈–70 kJ mol^{-1}). However, in combination with ${}^{13}\varepsilon_{CO_2\text{-}CH_4}$ and ${}^{2}\varepsilon_{CH_4\text{-}H_2O}$ data, the position in the ΔG_{net} landscape and the degree of departure from equilibrium may be uniquely constrained (Fig. 3). The multiple-isotope composition of methane may thus be a useful proxy for ΔG_{net} in natural environments where measurements of H_2, CO_2 and CH_4 concentrations are not easily obtainable. In addition to departure from equilibrium of the Mcr- and Mtr-catalyzed reactions, which may cause anti-clumped $\Delta^{12}CH_2D_2$ compositions, a testable prediction of our model is that the Hmd-catalyzed reaction may also cause anti-clumping. This arises from combinatorial effects (*30–32*) when Hmd activity is high, and especially during H_2-H_2O hydrogen isotopic disequilibrium (fig. S6).

The metabolic-isotopic model may be used to examine the controls on the isotopic fractionation of methanogenesis not only in laboratory cultures, but in natural environments as well. Laboratory cultures operate far from equilibrium, usually at H_2 concentrations and cell-specific methanogenesis rates (csMR) much higher than those in natural environments (table S5; fig. S9). Recent reevaluations of slowly forming biogenic methane sources such as marine sediments, coalbeds or shale gas deposits, revealed that apparent CH_4–CO_2 and CH_4–H_2O isotopic equilibrium is common (*8*,

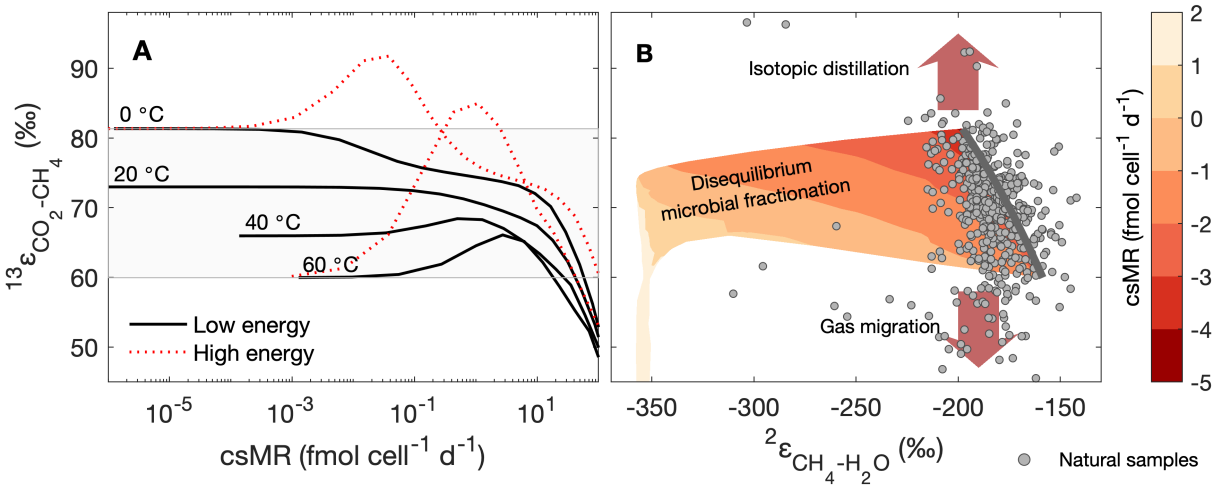

Figure 4: Isotopic fractionation during methanogenesis in energy-limited conditions. (**A**) $^{13}\varepsilon_{CO_2\text{-}CH_4}$ against csMR. Dotted red lines show the laboratory-calibrated model (high energy) results for the same temperatures. (**B**) $^{13}\varepsilon_{CO_2\text{-}CH_4}$ against $^{2}\varepsilon_{CH_4\text{-}H_2O}$. Contours are $\log_{10}$(csMR) predicted by our model, between 0°C and 60°C. The calculations are for [H_2] between 1 nM and 5 μM, [CO_2] and [CH_4] of 1 mM, and a cell volume of 1 μm^3. The circles are biogenic environmental samples from marine sediments, coalbed methane and natural gas deposits (n = 491).

21, *33–36*). There are currently no laboratory cultures that reproduce the isotopic effects associated with these conditions. We modified the model to use enzyme activities that were measured in H_2-limited laboratory cultures (SM) and assessed the resulting ΔG_{net}–csMR–isotopic relations at 0-60°C.

Existing estimates of environmental ΔG_{net} are more positive than –30 kJ mol^{-1} (table S5). However, the determination of ΔG_{net} in natural environments is often difficult because of low and spatially heterogeneous in-situ H_2 concentrations (*37–39*), and the actual range of ΔG_{net} likely reflects this heterogeneity. As ΔG_{net} determines the csMR (fig. S9), which is easier to measure, we henceforth discuss csMR–isotopic fractionation relations. In contrast to methanogenesis in lab cultures, we found that under energy-limited conditions, the Mtr-catalyzed reaction departs from equilibrium before the Mcr-catalyzed reaction (fig. S7). As a consequence, different csMR–fractionation relations emerge, most notably for $^{13}\varepsilon_{CO_2\text{-}CH_4}$ (Fig. 4A). Instead of an increase in $^{13}\varepsilon_{CO_2\text{-}CH_4}$ to larger-than-equilibrium values, $^{13}\varepsilon_{CO_2\text{-}CH_4}$ remains approximately constant up to csMR of ∼10 fmol cell^{-1} d^{-1}. The reason for this apparent carbon isotopic equilibrium is the similar magnitude of the EFF and KFF of Mtr (17‰ and 16‰ at 60°C, respectively, SM). An environmental predic-

tion of the above is that $^{13}\varepsilon_{CO_2\text{-}CH_4}$ that differs measurably from $^{13}\varepsilon^{eq}_{CO_2\text{-}CH_4}$ indicates csMR higher than $\sim$10 fmol cell^{-1} d^{-1}.

Analytically distinguishable departure of $^{2}\varepsilon_{CH_4\text{-}H_2O}$ from equilibrium occurs at csMR between $\sim$0.001 and 0.1 fmol cell^{-1} d^{-1} (at 0°C and 60°C, respectively; fig. S8B), and departure from clumped isotope equilibrium occurs over a similar range of csMR (fig. S8C, D). Thus, our model reveals that at csMR between 0.1 and 10 fmol cell^{-1} d^{-1}, one might expect near-equilibrium $^{13}\varepsilon_{CO_2\text{-}CH_4}$ concurrent with disequilibrium $^{2}\varepsilon_{CH_4\text{-}H_2O}$. The opposite situation (i.e., near-equilibrium $^{2}\varepsilon_{CH_4\text{-}H_2O}$ and disequilibrium $^{13}\varepsilon_{CO_2\text{-}CH_4}$) is common in natural environments, though csMR is usually unknown (fig. S9). As previously suggested, this apparent hydrogen isotopic equilibrium concurrent with carbon isotopic disequilibrium may be explained by diffusive mixing of CO_2 and CH_4, isotopic (Rayleigh) distillation, or diagenetic isotope exchange without net methane production (*8*, *34*, *40*, *41*, Fig. 4B). If disequilibrium $^{13}\varepsilon_{CO_2\text{-}CH_4}$ is explained as above rather than by microbial expression of KFFs, then the scarcity of data within the field representing disequilibrium microbial fractionation in Fig. 4B may reflect near-equilibrium isotopic fractionation during methanogenesis in energy-limited environments. This implies csMR lower than $\sim$0.001–0.1 fmol cell^{-1} d^{-1}(depending on temperature), consistent with almost all csMR estimated from cell abundances and volumetric methanogenesis rates (SM, table S6). In energy-limited environments with higher csMR, near-equilibrium $^{2}\varepsilon_{CH_4\text{-}H_2O}$ concurrent with disequilibrium $^{13}\varepsilon_{CO_2\text{-}CH_4}$ may be explained by methane cycling or anaerobic oxidation of methane that operates close to the thermodynamic limit (*42*).

By accounting for the metabolites and reactions in the hydrogenotrophic methanogenesis pathway, we link environmental substrate and product concentrations, pH and temperature to the energetics and net rate of methanogenesis, and to the associated fractionation of carbon, hydrogen and clumped isotopes. The landscape of departure of individual reactions in the pathway from reversibility controls these fractionations, explaining rate–fractionation relations in laboratory cultures, and highlighting the potential of multiple-isotope measurements of biogenic methane (carbon, hydrogen and clumped) as probes of the in-situ energetics of methanogenic activity.

Acknowledgments

J.G. acknowledges support from the Sustainability and Energy Research Initiative (SAERI) of the Weizmann Institute of Science. Q.J. is supported by NSF award EAR-1636815.

Author contributions

J.G. and I.H. conceived the study, developed and analyzed the metabolic-isotopic model, and wrote the initial draft. Q.J. developed the metabolic model. All authors contributed to the writing.

References

1. M. Saunois *et al.*, *Earth Syst. Sci. Data* **8**, 697–751, ISSN: 1866-3516 (Dec. 2016).
2. S. Schwietzke *et al.*, *Nature* **538**, 88–91, ISSN: 0028-0836 (Oct. 2016).
3. Z. Lyu, N. Shao, T. Akinyemi, W. B. Whitman, en, *Current Biology* **28**, R727–R732, ISSN: 0960-9822 (July 2018).
4. M. J. Whiticar, *Chem. Geol.* **161**, 291–314, ISSN: 00092541 (Sept. 1999).
5. E. G. Nisbet *et al.*, *Glob. Biogeochem. Cycles* **30**, 1356–1370, ISSN: 08866236 (Sept. 2016).
6. D. A. Stolper *et al.*, *Geochim. Cosmochim. Acta* **126**, 169–191, ISSN: 00167037 (Feb. 2014).
7. D. T. Wang *et al.*, *Science* **348**, 428–431, ISSN: 1095-9203 (Apr. 2015).
8. T. Okumura *et al.*, *Prog. Earth Planet. Sci.* **3**, 14, ISSN: 2197-4284 (Dec. 2016).
9. X. Cao, H. Bao, Y. Peng, *Geochim. Cosmochim. Acta* **249**, 59–75, ISSN: 0016-7037 (Jan. 2019).
10. J. Bassham, G. Krause, en, *Biochim. Biophys. Acta BBA - Bioenerg.* **189**, 207–221, ISSN: 0005-2728 (Oct. 1969).
11. D. A. Beard, H. Qian, *PloS One* **2**, e144, ISSN: 1932-6203 (Jan. 2007).
12. E. Noor, A. Flamholz, W. Liebermeister, A. Bar-Even, R. Milo, *FEBS Lett.* **587**, 2772–7 (Sept. 2013).

13. C. Rees, *Geochim. Cosmochim. Acta* **37**, 1141–1162, ISSN: 00167037 (May 1973).

14. B. A. Wing, I. Halevy, *Proc. Natl. Acad. Sci. U. S. A.* **111**, 18116–25, ISSN: 1091-6490 (Dec. 2014).

15. D. L. Valentine, A. Chidthaisong, A. Rice, W. S. Reeburgh, S. C. Tyler, *Geochim. Cosmochim. Acta* **68**, 1571–1590, ISSN: 00167037 (Apr. 2004).

16. H. Penning, C. M. Plugge, P. E. Galand, R. Conrad, *Glob. Change Biol.* **11**, 2103–2113, ISSN: 1354-1013 (Dec. 2005).

17. K. Takai *et al.*, *Proc. Natl. Acad. Sci. U. S. A.* **105**, 10949–54, ISSN: 1091-6490 (Aug. 2008).

18. S. Hattori *et al.*, *Geochem. J.* **46**, 193–200, ISSN: 00167002 (2012).

19. B. D. Topçuoğlu, C. Meydan, T. B. Nguyen, S. Q. Lang, J. F. Holden, *Appl. Environ. Microbiol.* **85**, 1–14, ISSN: 0099-2240 (Mar. 2019).

20. S. Scheller, M. Goenrich, R. K. Thauer, B. Jaun, *J. Am. Chem. Soc.* **135**, 14975–84, ISSN: 1520-5126 (Oct. 2013).

21. J. Gropp, M. A. Iron, I. Halevy, en, *Geochimica et Cosmochimica Acta* **295**, 237–264, ISSN: 0016-7037 (Feb. 2021).

22. H. M. Miller *et al.*, *Geochim. Cosmochim. Acta* **237**, 18–31, ISSN: 00167037 (June 2018).

23. D. B. Nothaft *et al.*, en, *J. Geophys. Res. Biogeosciences* **NA**, e2020JG006025, ISSN: 2169-8961 (2021).

24. H. Yoshioka, S. Sakata, Y. Kamagata, *Geochim. Cosmochim. Acta* **72**, 2687–2694, ISSN: 00167037 (2008).

25. S. Kawagucci *et al.*, *Geochim. Cosmochim. Acta* **142**, 601–614, ISSN: 00167037 (Oct. 2014).

26. C. Afting, E. Kremmer, C. Brucker, A. Hochheimer, R. K. Thauer, *Arch. Microbiol.* **174**, 225–232, ISSN: 0302-8933 (Sept. 2000).

27. R. Botz, H. D. Pokojski, M. Schmitt, M. Thomm, *Org. Geochem.* **25**, 255–262, ISSN: 0146-6380 (1996).

28. P. M. Douglas *et al.*, *Org. Geochem.* **113**, 262–282, ISSN: 01466380 (Nov. 2017).

29. D. A. Stolper *et al.*, *Geochim. Cosmochim. Acta* **161**, 219–247, ISSN: 00167037 (July 2015).

30. L. Y. Yeung, *Geochim. Cosmochim. Acta* **172**, 22–38, ISSN: 00167037 (Jan. 2016).

31. T. Röckmann, M. E. Popa, M. C. Krol, M. E. G. Hofmann, *Sci. Rep.* **6**, 31947, ISSN: 2045-2322 (Oct. 2016).

32. L. Taenzer *et al.*, en, *Geochimica et Cosmochimica Acta* **285**, 225–236, ISSN: 0016-7037 (Sept. 2020).

33. D. S. Vinson *et al.*, *Chem. Geol.* **453**, 128–145, ISSN: 00092541 (2017).

34. A. C. Turner *et al.*, en, *Geochimica et Cosmochimica Acta* **NA**, NA, ISSN: 0016-7037 (Apr. 2021).

35. J. J. Jautzy, P. M. J. Douglas, H. Xie, J. M. Eiler, I. D. Clark, en, *Earth and Planetary Science Letters* **562**, 116841, ISSN: 0012-821X (May 2021).

36. N. Zhang *et al.*, en, *Geochimica et Cosmochimica Acta* **NA**, NA, ISSN: 0016-7037 (Aug. 2021).

37. R. Conrad, T. J. Phelps, J. G. Zeikus, *Appl. Environ. Microbiol.* **50**, 595–601, ISSN: 0099-2240 (Sept. 1985).

38. E. Giraldo-Gomez, S. Goodwin, M. S. Switzenbaum, *Biotechnol. Bioeng.* **40**, 768–76, ISSN: 0006-3592 (Oct. 1992).

39. Y.-S. Lin *et al.*, en, *Geochimica et Cosmochimica Acta* **77**, 186–201, ISSN: 0016-7037 (Jan. 2012).

40. C. K. Paull *et al.*, *Proc. Ocean Drill. Program Sci. Results* **164**, 67–78 (2000).

41. J. W. Pohlman, M. Kaneko, V. B. Heuer, R. B. Coffin, M. Whiticar, en, *Earth and Planetary Science Letters* **287**, 504–512, ISSN: 0012-821X (Oct. 2009).

42. G. Wegener, J. Gropp, H. Taubner, I. Halevy, M. Elvert, en, *Sci. Adv.* **7**, eabe4939, ISSN: 2375-2548 (May 2021).